PAPER

Design principles for superamphiphobic surfaces

Hans-Jürgen Butt,[*a] Ciro Semprebon,[b] Periklis Papadopoulos,[a] Doris Vollmer,[a] Martin Brinkmann[bc] and Matteo Ciccotti[d]

To predict the properties of superamphiphobic layers we analyzed the wetting of a square and a hexagonal array of vertical pillars composed of spheres (radius R) partially sintered together. Apparent contact angles above $150°$ are obtained by pinning of a non-polar liquid surface at the underside of the top sphere resulting in a Fakir or Cassie state. Analytical equations are derived for the impalement pressure in the limiting case $A_0 \gg R^2$, where A_0 is the area of the regular unit cell containing a single pillar. The case of close pillars is investigated numerically. By balancing forces at the rim of a drop, we calculate the apparent receding contact angle. To describe drag reduction of a flowing liquid we calculate the apparent slip length. When considering pressure-induced flow through cylindrical capillaries of radius r_c, significant drag reduction occurs only for thin capillaries. The mechanical stability with respect to normal forces and shear is analyzed. Nanoscopic silica glass pillars would be able to sustain the normal and shear stresses caused by capillary and drag forces. For a high impalement pressure and good mechanical stability A_0 should be small and R (respectively the neck diameter) should be large, whereas a large A_0 and a small R imply low contact angle hysteresis and high slip length.

Introduction

Superhydrophobic surfaces are defined by a contact angle with water of $150°$ or higher and a sliding or roll-off angle below 5–$10°$. Superhydrophobic surfaces have been made in different ways and they have been analyzed extensively. The interest is to a large extent driven by their potential applications as self-cleaning or antifouling coatings.[1] In addition, superhydrophobic surfaces can reduce hydrodynamic drag of water.[2–8]

Superhydrophobicity is based on two principles:[9] a low surface energy of the solid surface, usually by coating the surface with a fluorinated hydrocarbon, and an increased surface roughness, for example by micropatterning. One model superhydrophobic layer is a regular array of pillars, which are chemically modified to render them hydrophobic. To reach apparent contact angles above $150°$ and a contact angle hysteresis below $5°$ the superhydrophobic layers are usually designed in a way that air is entrained and the drop is suspended on top of the pillars. This is called the Cassie or Fakir state (Fig. 1A).

The apparent, macroscopic contact angle Θ^{app} of the liquid observed on a length scale much larger than the scale of the microstructures and the material contact angle Θ are traditionally related by the Cassie–Baxter equation:[10,11]

$$\cos \theta^{app} = r\varphi_s \cos \theta - (1 - \varphi_s) \tag{1}$$

here φ_s and $(1 - \varphi_s)$ are the area fractions of the projected liquid–solid and liquid–vapor interface, respectively. The Wenzel factor $r \geq 1$ is the ratio of true to projected area of the wet substrate. It accounts for the non-flat surface topography of the pillars.[12]

The Cassie–Baxter model (eqn (1)) is derived from a balance of interfacial and surface energies assuming that the Cassie state is at least metastable. Under certain conditions, however, the Cassie state may become unstable causing the liquid to penetrate the space in between the pillars. This impalement transition into the so-called Wenzel state can be observed if the pressure difference between liquid and vapor phases exceeds a certain threshold value.
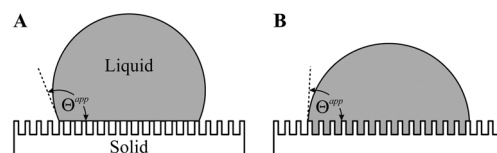
[a]*Max Planck Institute for Polymer Research, Ackermannweg 10, D-55128 Mainz, Germany. E-mail: butt@mpip-mainz.mpg.de*

[b]*Dept. Complex Fluids, Max Planck Institute for Dynamics and Self-Organization, Am Faßberg 17, 37077 Göttingen, Germany*

[c]*Experimental Physics, Saarland University, 66123 Saarbrücken, Germany*

[d]*Laboratoire PPMD/SIMM, UMR 7615 (CNRS, UPMC, ESPCI Paristech), 10 rue Vauquelin, 75005 Paris, France*

Fig. 1 Schematic of a sessile drop on an array of pillars in the Cassie (A) and Wenzel state (B).

Superamphiphobic surfaces show high contact angles (>150°) and low sliding angles (<5 to 10°) with water and non-polar liquids,[13,14] extending the advantages of superhydrophobic surfaces to oily liquids. They are less prone to contamination, so potential applications are for antifouling coatings and for drag reduction.[1] To make superamphiphobic surfaces it is not sufficient to use materials with low surface energy and roughen the surface. Since no oil shows a Young's contact angle above 90° with any planar solid surface, overhanging structures are required to fabricate superamphiphobic surfaces.[14,15] Because of this additional requirement it is more difficult to fabricate superamphiphobic surfaces than superhydrophobic ones. Strategies employed are either spontaneous bottom-up,[13,16–20] lithographic top-down,[14,21] or combined approaches.[22–24] The bottom-up approach is usually technically less demanding, potentially simpler, more likely to be defect-free, and extends to sub-100 nm building blocks. In particular, structures consisting of regular arrays of differently shaped regular structures of pre-determined shape and size have been made to address fundamental questions.[11,25–28] Also, overhanging structures formed by fibrous structures have been considered.[29,30]

Many superhydrophobic and superamphiphobic surfaces are made of (or terminate in) spherical structural elements.[17–20,23,31] To better understand superamphiphobicity, we consider a model structure made of spheres all of similar radius R. The spheres are supposed to be sintered together and form vertical pillars, assumed to be arranged in a two-dimensional regular pattern. A non-polar liquid on top of any superamphiphobic layer is only metastable; once the liquid impales between the pillars and wets the bottom surface it remains there. This is the Cassie-to-Wenzel or impalement transition and must be prevented to preserve the superamphiphobic properties. We consider the simplest case, that of a liquid, *e.g.* a drop, carefully placed on a superamphiphobic structure. First, we calculate the impalement pressure. That is the maximum pressure allowed by the geometrical constraints of the pattern before the Cassie state collapses and the liquid changes to the Wenzel state. Pressure may be exerted by the capillary pressures of a sessile drop or an external hydrostatic pressure. Second, we relate the microscopic parameters, in particular the material contact angle Θ, to the apparent advancing and receding contact angles Θ_a^{app} and Θ_r^{app}. Third, we calculate the mechanical resistance of the layer to shear stress. Fourth, we consider hydrodynamic flow of a liquid through a tube or capillary coated at the inside with a superamphiphobic layer. We calculate the apparent slip length from microscopic parameters and relate it to drag reduction and flow enhancement.

Designing superhydrophobic surfaces has been described in a number of publications (*e.g.* ref. 25, 26 and 32–34). With respect to systematically designing superamphiphobic layers we are only aware of few publications.[5,15,21,35–37] The aim of this paper is to help in designing superamphiphobic layers with high apparent contact angles, which are mechanically stable and show reduced hydrodynamic drag. Not all of these parameters can be optimized at the same time and compromises have to be reached. The aim is also to identify the fundamental, physical limits of superamphiphobicity. In order to overcome these limits, new fundamental principles of superamphiphobicity have to be invoked.

Theory

Overview and definitions

On nano- or microstructured superamphiphobic surfaces it is necessary to distinguish between intrinsic (microscopic) contact angles of the material and macroscopic, apparent contact angles of the structured surface. We term the contact angle measured on a homogeneous planar surface of a certain material, the *material* contact angle Θ. This is the contact angle formed by the liquid when extrapolating the liquid shape on the 10 nm to 1 μm scale to the interface. We neglect the effect of interfacial forces, which may influence the shape of the liquid interface on the 10 nm scale close to the contact line.[38] On an ideal smooth surface the material contact angle would be described by the Young's relation. It is well known that on real surfaces the contact angle for an advancing liquid is larger than the one for a receding liquid, also if the surfaces are smooth, and chemically homogeneous, *etc.* Therefore we distinguish, even on the microscopic length scale, between advancing Θ_a and receding material contact angles Θ_r.

The macroscopic scale in this manuscript is the length scale observed by eye or with a low-resolution microscope. It is much larger than the nano- and microstructures forming the superamphiphobic layer, thus typically larger than 10 μm. On the macroscopic length scale we discriminate between *apparent* advancing and *apparent* receding contact angles, denoted by Θ_a^{app} and Θ_r^{app}, respectively, and related to them the details of the underlying pattern. We also discriminate between the *three phase contact line* (or simply contact line) on the microscopic and the *rim* on the macroscopic length scale.

In the following we assume that the pressure difference is not related to any specific situation and is rather externally controlled. Note that the theory presented here does not apply to impalement of evaporating sessile drops with a lateral size on the order of the lattice spacing. When considering evaporating drops one should consider that the Laplace pressure in the drop increases with time.

Let us consider an array of pillars of particles all of equal radius R arranged in a rectangular lattice of lattice constant a (Fig. 2). The particles are supposed to be sintered together. The position of the connecting part is characterized by the angle β. Each pillar has N particles so that the total height of each pillar is $H_0 = (2N - 1)R\cos\beta$, neglecting the cap of the top sphere. Without any external pressure, the non-polar liquid surface
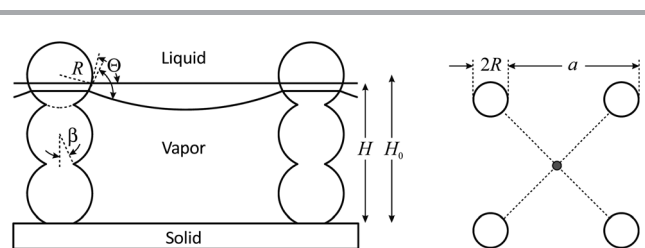

Fig. 2 Schematic of the superamphiphobic layer consisting of pillars of sintered spheres from side and top view. The liquid is suspended on top in the Cassie state. If no pressure is applied, the liquid surface is planar. With pressure the contact line moves downwards and the interface starts to curve.

would form a perfectly planar interface at a height $H = (2N − 1)$ $R\cos\beta − R\cos\Theta$.

The impalement pressure for spaced pillars

There are two possible mechanisms leading to the Cassie-to-Wenzel transition induced by an applied pressure. First, the curvature of the liquid interface could reach a value set by the geometry of the pattern such that the liquid touches the substrate (sag impalement).[26,39,40] Second, the liquid–air interface could depin from the top sphere and move downwards (depinning impalement).[5,8,34]

SAG IMPALEMENT. If the pillars are high $(H > a/\sqrt{2})$ the sag pressure is related to the maximum pressure allowed by the geometry of the system. For a square lattice the largest possible value of the mean curvature must be related to the diagonal distance of the pillars, being roughly $a\sqrt{2}$ in case $R \ll a$. Assuming that the profile of the liquid surface can be approximated by circular arcs, the largest possible curvature is attained for a semicircle centered at the top level of the pillars. With the Laplace equation relating the mean curvature to the pressure difference P between liquid and vapor phases and the interfacial tension γ, we arrive at a maximum pressure:

$$P = \frac{4}{\sqrt{2}}\frac{\gamma}{a} \qquad (2)$$

In the case of low pillars $H < a/\sqrt{2}$ the liquid interface can touch the bottom of the substrate, which effectively lowers the limiting pressure to:

$$P = \frac{8\gamma H}{a^2 + 2H^2} \qquad (3)$$

IMPALEMENT DUE TO DEPINNING. We compute the maximum pressure difference that the interface in an array of pillars can sustain without going to the Wenzel state. Therefore, first the maximum force on a single pillar is calculated. Then we estimate the maximum pressure from this force and the area of a unit cell. On each pillar the liquid interface exerts a capillary force given by the line integral of the vertical component of the tension of the liquid–vapor interface along the contact line. This force has also been calculated in the context of the particle–bubble interaction in flotation and sphere tensiometry.[41–43] In the case of large pillar spacing $(R \ll a)$ we can assume the liquid–air interface having rotational symmetry, and the capillary force is given by[44]

$$F_c = 2\pi\gamma R\sin\alpha\sin(\Theta_a − \alpha) \qquad (4)$$

here α is the angle describing the position of the contact line on the particle surface (Fig. 3). We employ the material advancing contact angle Θ_a since the liquid is advancing on the surface of the pillar.

When $\alpha = \Theta_a/2$ the force in eqn (4) is maximum and is expressed by[41–43]

$$F_c = 2\pi\gamma R\sin^2\frac{\Theta_a}{2} \qquad (5)$$

In mechanical equilibrium the capillary force has to be equal to the pressure P multiplied by the area A of the liquid–air
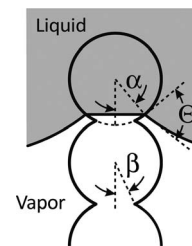

Fig. 3 Schematic of the top of a pillar with the liquid interface.

interface per pillar projected into the plane of the substrate: $F_c = PA$. In the limit of large pillar spacing, $R \ll a$, we can replace A by the total area A_0 per pillar. In this approximation the pressure and the capillary force reach their maximum simultaneously. The depinning impalement pressure is

$$P = \frac{2\pi\gamma R}{A_0}\sin^2\frac{\Theta_a}{2} \qquad (6)$$

For the unit cell of a square lattice, we have $A_0 = a^2$. For a hexagonal arrangement of pillars the area is $A_0 = a^2\sqrt{3}/2$. Eqn (5) and (6) are only valid if the liquid surface does not touch the second sphere from the top. As long as $\beta < \Theta_a/2$ this is most likely the case, even though for non-polar liquids the contact angle is below 90°. For $\beta > \Theta_a/2$ we have to derive the depinning pressure directly from eqn (4) with $\alpha = \beta$.

In Fig. 4A the impalement pressure calculated with eqn (6) is compared to the one calculated with eqn (2) and (3); we chose $\gamma = 0.04$ N m^{-1} and $\Theta_a = 70°$ as typical parameters. Calculations were carried out for $R = 50$ nm, 0.5 μm and 5 μm. Results can accordingly be only shown for $a > 100$ nm, 1 μm and 10 μm, respectively. The depinning impalement pressure is lower than the impalement pressure due to sagging for high pillars calculated with eqn (2). It scales with a^{-2} rather than a^{-1}. As a consequence depinning rather than sagging limits the performance. This is further demonstrated by calculating the sagging impalement pressure for pillars of only two spheres taking $H = R[3\cos\beta − \cos(\Theta_a/2)]$ (dotted lines; eqn (3)). In each curve two regimes with different scaling are obtained. For low spacing the impalement pressure decreases with a^{-1} as for high pillars. For large spacing the decrease is proportional to a^{-2}. Even for the case of only two spheres in one pillar, depinning occurs at a lower pressure than sagging. Practically, reducing the pillar height to only two spheres may, however, not be robust enough. Even a slight flow or a soft impact may cause a Cassie-to-Wenzel transition.

Impalement pressure for close pillars

If the density of pillars is high and $2R \ll a$ is not fulfilled, one has to account for two effects. First, the true projected area of the liquid–air interface has to be employed, i.e., the area of the unit cell corrected by the area enclosed by the projected contour of the contact line. Second, the three dimensional contour of the three phase contact line on a pillar becomes more and more distorted and non-circular as $a \to 2R$. Hence, the simple geometric model does not hold anymore. The expression accounting for the first effect is:

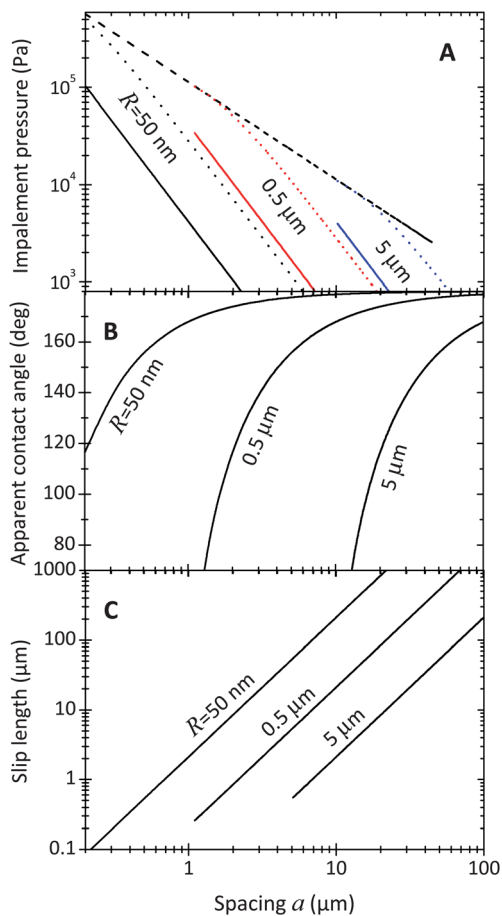**Fig. 4** (A) Impalement pressure *versus* spacing *a* between pillars calculated with eqn (2) for sagging (dashed line) with high pillars, sagging for pillars with only two spheres calculated with eqn (3) (dotted lines), and for depinning (continuous lines) calculated with eqn (6) for different particle sizes. (B) Apparent receding contact angle calculated with eqn (11). (C) Slip length *versus* spacing calculated with eqn (30) using $f = 0.5$. Parameters: $R = 50$ nm, 0.5 μm, and 5 μm, $\gamma = 0.04$ N m^{-1}, $\Theta_a = 70°$, $\beta = 30°$.

$$P = \frac{2\pi\gamma R \sin\,\alpha \sin(\Theta_a - \alpha)}{A_0 - \pi R^2 \sin^2\alpha} \qquad (7)$$

The pressure maximum is shifted to larger values $\alpha > \Theta_a/2$ of the opening angle as the effective area becomes smaller when the contact line moves down the pillar. The opening angle for maximum pressure ($\mathrm{d}P/\mathrm{d}\alpha = 0$) is given by

$$\sin\alpha = a\sqrt{\frac{2a^2 - R^2\sin^2\Theta_a - 2a\cos\Theta_a\sqrt{a^2 - R^2\sin^2\Theta_a}}{(R^2 - 2a^2)^2 + R^2(4a^2 - R^2)\cos\Theta_a}} \qquad (8)$$

The value of the pressure at its maximum is larger than the impalement pressure predicted by eqn (6) (Fig. 5). It can be calculated by inserting α obtained from eqn (8) into (7).

To determine the maximum pressure for close arrangements of pillars, we performed numerical minimizations of the interfacial energy. Here, we used the freely available software surface evolver.[45] Regular square and hexagonal lattices of pillars were considered. For both geometries we impose the condition that the liquid–air interface is horizontal on the boundaries of the

domains while the interface can move freely up and down on the sidewalls. This boundary condition is a direct consequence of the reflection symmetry of the liquid–air interface on the boundary of the unit cell.

Results are summarized in Fig. 5 for material contact angles of $\Theta_a = 70°$ and $\Theta_a = 120°$. The normalized pressure is plotted *versus* the normalized spacing. The normalized spacing is $\sqrt{A_0}/R$, where A_0 is the area of the unit cell containing a single pillar. Thus for a square lattice the normalized spacing is a/R and for the hexagonal lattice it is $3^{-1/4}a/R$. A comparison of the model calculations shows that as expected the impalement pressure derived by maximizing the force (eqn (6)) and the effective pressure (eqn (7) and (8)) is asymptotically identical for $a/2R \to \infty$. In the opposite limit, for $a/2R \to 1$ and $\Theta_a = 70°$, the approximation (6) underestimates the impalement pressure by a factor of up to two smaller than the maximum of expression (7). For $\Theta_a = 120°$ eqn (7) diverges in the limit $a/2R \to 1$ due to the unphysical toroidal ring induced by the rotational symmetry. The snapshots of the liquid morphologies for small spacings close to the maximum pressure included in Fig. 5 help to clarify the situation: while for $\Theta_a = 70°$ the corrugation of the contact line is smooth, for $\Theta_a = 120°$ the contact line present large oscillations along the directions of the other spheres.

The numerical results for the square and hexagonal packing scale with a^{-2}. In the limit $a/2R \to 1$, they approach intermediate values between the maximum force and the maximum pressure criteria. These values are in good agreement with the imbibition and drainage pressure obtained for close spacing of
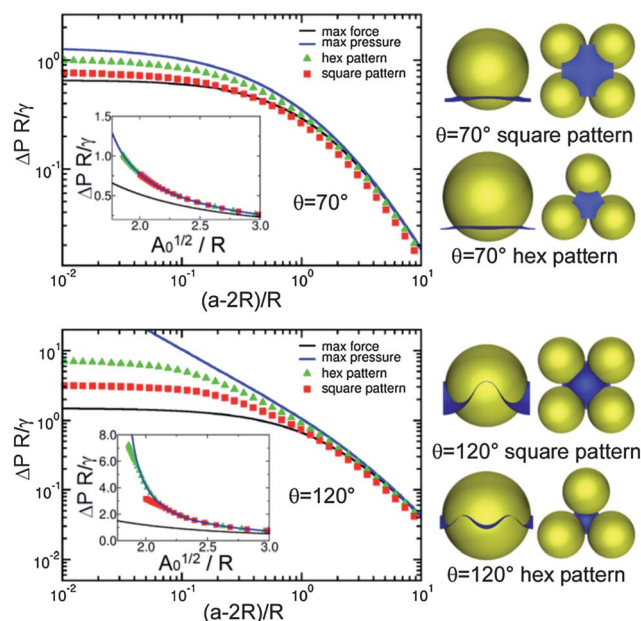

Fig. 5 Normalized impalement pressure due to interfacial depinning from pillars *versus* separation $s = a - 2R$ divided by the radius R for $\Theta_a = 70°$ and 120° and $\gamma = 0.04$ N m^{-1}. Solid lines display the maximum pressure according to eqn (7) and (8) (black) and the maximum pressure in eqn (6) (blue). Symbols indicate the data obtained from numerical minimizations of the interfacial energy for the square (red squares) and hexagonal (green hexagons) geometry. The insets show the normalized depinning pressure *versus* the normalized size. The normalized size is $\sqrt{A_0}/R$, where A_0 the area of the unit cell containing a single pillar.

spheres with the same geometries.[46,47] As shown in Fig. 5, the numerically obtained data for the square and hexagonal lattices and the analytical results for maximum pressure according to eqn (7) and (8) collapse onto the same master curve. Only in the case of a large material contact angle $\Theta_a = 120°$, we find a noticeable deviation which is due to the formation of pendular bridges between the points of close contact. The maximum pressure according to the maximum force criterion in eqn (6), however, systematically underestimates the maximum pressure and approaches the numeric results only asymptotically for large separations.

Material and apparent contact angles

To relate the two contact angles we consider the situation at the rim of a drop (Fig. 6). The drop is supposed to be large enough so that the distance between pillars is much smaller than the radius of the drop. The topmost sphere at the rim just before the rim detaches experiences a force in the direction of the movement of the rim of

$$F_r = 2\pi\gamma R\sin^2\left(\frac{\pi - \Theta_r}{2}\right) = 2\pi\gamma R\cos^2\frac{\Theta_r}{2} \quad (9)$$

This equation is fundamentally the same as eqn (5), we only replaced the contact angle by $\pi - \Theta_r$ because the liquid is pulled away from the sphere. The outward force caused by the Laplace pressure can usually be neglected. F_r is acting in a direction $\Theta_r^{app}/2$ with respect to the horizon (Fig. 6). The horizontal inward component of this force is

$$F_h = 2\pi\gamma R\cos^2\frac{\Theta_r}{2}\cos\frac{\Theta_r^{app}}{2} \quad (10)$$

When the rim recedes the liquid detaches from the topmost sphere of the pillar and is then pinned at the top sphere of the next pillar to the right. Just before the liquid recedes macroscopically this horizontal component is balanced by the surface tensional force per unit length $\gamma(1 + \cos\Theta_r^{app})$. If we equate both for a line parallel to the rows of pillars we get

$$\Theta_r^{app} = 2\cdot\arccos\left(\frac{\pi R}{a}\cos^2\frac{\Theta_r}{2}\right) \quad (11)$$

We used the mathematical identity $(1 + \cos x)/\cos(x/2) = 2\cos(x/2)$. If the argument is much smaller than unity ($R/a \ll 1$), the arccos can be written in a series: $\arccos(x) = \pi/2 - x \pm \dots$ leading to
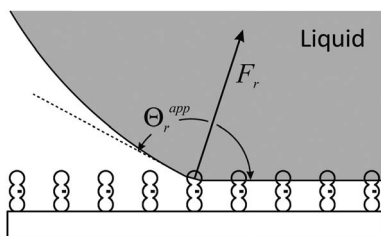
$$\Theta_r^{app} = \pi\left(1 - \frac{2R}{a}\cos^2\frac{\Theta_r}{2}\right) \quad (12)$$

Eqn (11) and (12) allow us to relate the materials contact angle to the apparent contact angle for a liquid surface with a rim moving perpendicular to rows of pillars, i.e. in the (1,0) or (0,1) direction.

We can draw several conclusions:
• With respect to the shape of the superamphiphobic layer the apparent receding contact angle only depends on the ratio a/R. For a given Θ_r, the ratio a/R should be as high as possible to achieve a high apparent receding contact angle (Fig. 4B).
• The apparent contact angle increases with the material contact angle (Fig. 7). The dependence of Θ_r^{app} on Θ_r is, however, weak. The higher the ratio a/R the weaker the dependence of Θ_r^{app} on Θ_r.
• The surface tension γ does not directly appear in eqn (11). The surface tension enters indirectly via the material contact angle and Young's equation.

On two-dimensional arrays of pillars the apparent contact angles depend on the direction. The larger the spacing in a given direction the higher the apparent receding contact angles. For example, if we consider the rim moving in the (1,1) direction, that is 45° with respect to rows of pillars, the spacing between rows is $a\sqrt{2}$ and eqn (11) becomes

$$\Theta_r^{app} = 2\cdot\arccos\left(\frac{\pi R}{a\sqrt{2}}\cos^2\frac{\Theta_r}{2}\right) \quad (13)$$

For comparison we also applied the Cassie–Baxter equation (eqn (1)) to relate the materials contact angle to the apparent contact angle (Fig. 7). From the geometry the projected area of the liquid–solid interface is given by $\varphi_s = \pi R^2\sin^2\Theta_r/a^2$ and the curvature correction by $r = 2(1 + \cos\Theta_r)/\sin^2\Theta_r$. Combining in eqn (1) and rearranging we obtain

$$\cos\Theta_r^{app} = \frac{\pi R^2}{a^2}(1 + \cos\Theta_r)^2 - 1 \quad (14)$$

The Cassie–Baxter equation leads to significantly higher apparent contact angles than those obtained with eqn (11). The
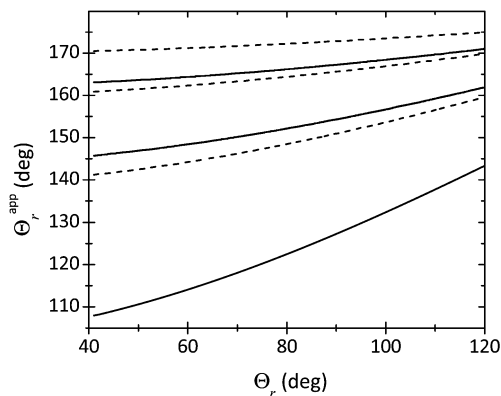

Fig. 6 Schematic of the left rim of a receding liquid drop on a superamphiphobic layer.

Fig. 7 Apparent receding contact angle versus the material receding contact angle for $a/R = 5$, 10, and 20 from bottom to top. Θ_r^{app} was calculated with eqn (11) (continuous lines). For comparison, the apparent contact angle was also calculated with the Cassie–Baxter equation (eqn (14)) (dashed lines).

relevant factor scales with the respective area covered by pillars, R^2/a^2, rather than R/a. The Cassie–Baxter equation is not applicable because any shift of the rim is discontinuous and determined by horizontal depinning.[32,48,49]

The advancing contact angle is solely given by geometry. For the liquid surface to advance it has to touch the top of the next neighboring pillar. As soon as it gets into contact with the next pillar, it is going to wet the top sphere. If all pillars have perfectly the same height and spacing, this happens when Θ_a^{app} reaches a critical value given by (Fig. 8)

$$\frac{R(1 + \cos \Theta_a)}{a} = \tan(\pi - \Theta_a^{app}) \Rightarrow$$
$$\Theta_a^{app} = \pi - \arctan\left[\frac{R}{a}(1 + \cos \Theta_a)\right] \quad (15)$$

Eqn (15) was derived on purely geometric grounds. Most likely, the contact is established significantly before. Thermal fluctuations, external mechanical noise, inhomogeneous height and position distributions of pillars will cause the liquid to get into contact with the neighboring pillar before. In particular when the drop is placed on the superamphiphobic surface or when one starts to tilt the plate, mechanical vibrations can easily cause the drop to fluctuate. Therefore, eqn (15) gives a higher limit. Practically, always the receding contact angle will dominate superamphiphobicity because the relevant question is to which degree does the drop detach after placing it on a surface and disturbing it mechanically.

Mechanical damage

We first consider the mechanical resistance of pillars constituted of silica glass to vertical stress. The critical vertical stress σ_{vp} inducing plastic yield of the pillars can be estimated as:

$$\sigma_{vp} = \frac{\sigma_y \pi r_p^2}{a^2} \quad (16)$$

here σ_y is the yield strength of the material constituting the pillar and r_p is the radius of the pillar. To estimate the radius r_p we treat the pillar as a circular beam with a radius $r_p = R \sin \beta$. The constitutive relation for plastic yielding in silica glass has recently been investigated by Lacroix et al.[50] on micron sized silica pillars. It provides an estimate of the yield strength under uniaxial compression of $\sigma_y = 6.5$ GPa. For example, with $a = 1$ μm, $R = 50$ nm, $\beta = 30°$ we obtain a critical vertical stress of $\sigma_{vp} = 13$ MPa.

The pillars are exposed to various mechanical stresses. Vertical stresses on the pillars in the Cassie state are mainly caus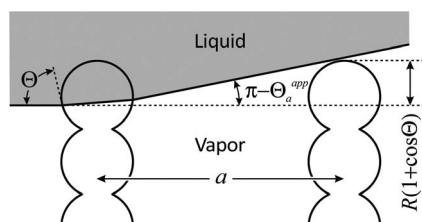ed by the pressure in the liquid, as it may be induced from the weight of a drop. Other sources of vertical stress are the impact of dust particles, drops, or touching the layer. Pillar failure originating from vertical compressive stresses can be due to either plastic yield or buckling. The critical buckling force for a pillar with one end fixed and the other end free to move laterally is

$$F_{vb} = \frac{\pi^2 EI}{4H_0^2} = \frac{\pi^3 E r_p^4}{16 H_0^2} \quad (17)$$

here, $I = \pi r_p^4/4$ is the moment of inertia for a cylindrical beam of radius r_p and E is the Young's modulus. The corresponding critical vertical stress for buckling is

$$\sigma_{vb} = \frac{F_{vb}}{a^2} = \frac{\pi^3 E r_p^4}{16 H_0^2 a^2} \quad (18)$$

For two examples the critical vertical stress versus pillar spacing is plotted in Fig. 9. The two examples are for $H_0 = 1$ μm and 350 nm, corresponding to 12 and 4 silica particles of 50 nm radius and $\beta = 30°$, respectively. Buckling occurs at lower vertical stress than yielding. We conclude that buckling is the most limiting failure mechanisms under vertical compression. This should generally be accounted for in the design of the pillars. However, the critical stress for buckling is higher than all estimates of the impalement pressure. Thus the hydrostatic pressure of the liquid is no concern for the present application, where the liquid should remain in the Cassie state.

Forces in the horizontal direction are more problematic. They can be caused by the drag of a flowing liquid, by horizontal capillary forces at the rim of a drop, or by the inertia of an impacting drop. They may also be caused by other sources not related to the liquid, for example when touching the super-amphiphobic layer.

When the pillars are equally spaced, the effect of a homogeneous, horizontal stress σ_h applied on the top of the super-amphiphobic layer results in a force $F_h = \sigma_h a^2$ applied on the top sphere of each pillar. The deflection δ of an elastic beam with a circular cross-section of radius r_p is related to the horizontal force $F_h = \sigma_h a^2$ by
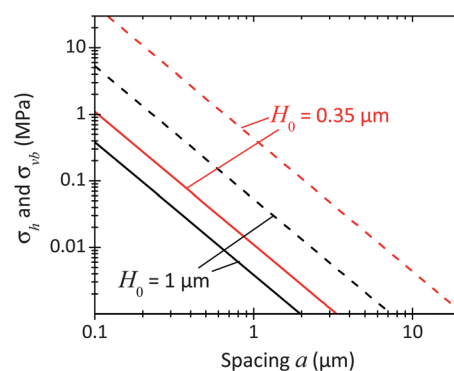

Fig. 8 Schematic of the advancing side of the rim of a liquid drop on an array of pillars.

Fig. 9 Critical vertical stress for buckling σ_{vb} (eqn (18); dashed lines) and critical value of the horizontal shear stress σ_h (eqn (22); continuous lines) versus spacing a for pillars of $H_0 = 1$ μm (black) and 350 nm (red) height. Other parameters were: $R = 50$ nm, $\beta = 30°$, $E = 70$ GPa, and $\sigma_R = 5$ GPa.

$$\delta = \frac{F_h}{EI} \frac{H_0{}^3}{3} \qquad (19)$$

The local stress condition in an elongated beam under flexion is essentially uniaxial. The maximum local tensile stress σ_{max} occurs at the external surface of the beam and close to the fixed basement. Its value is given by

$$\sigma_{max} = \frac{F_h H_0 r_p}{I} \qquad (20)$$

When expressed in terms of the homogeneous, horizontal shear stress σ_h this becomes:

$$\sigma_{max} = \frac{4}{\pi} \frac{\sigma_h a^2 H_0}{R^3 \sin^3 \beta} \qquad (21)$$

If the maximal stress exceeds the rupture strength, σ_R, the pillar breaks. The critical value of the horizontal shear stress σ_h is thus:

$$\sigma_h = \frac{\pi R^3 \sin^3 \beta}{4 H_0 a^2} \sigma_R \qquad (22)$$

From the mechanical point of view the pillars should thus be made of large spheres with a large neck size (high β). The pillars should be short and densely spaced. The rupture strength of the material should be as high as possible.

Estimating the maximal rupture strength σ_R depends on the particular material and on the failure mechanism, which may significantly be affected by the size of the considered object. According to Griffith's observations[51] the strength of oxide glasses at the macroscopic scale is strongly limited by the typical size c of defects, represented by everpresent microscale fractures originated during manufacture and handling. The failure mode is essentially given by the brittle fracture propagation originating from the largest defect in the stressed region. The rupture strength is related to the theoretical limiting fracture strength σ_{th} by $\sigma_R \approx 2\sigma_{th}\sqrt{c/\rho}$. Here, ρ is the curvature radius at the end of a microcrack. It is of molecular dimensions in glasses and the theoretical limiting strength is estimated to be $\sigma_{th} \approx 14$ GPa for silica glass.[52] Although the typical strength of window glass is only around 90 MPa, due to micron size defects, the strength of optical fibers of micron scale diameter bearing only nanoscale defects can reach 10 GPa in a vacuum and 5 GPa in the current atmosphere.[52] Recent measurements on silica nanowires confirm a further increase of strength beyond 10 GPa (ref. 53) just after formulation. For such small objects, the bearable defect size becomes of molecular order, and the fracture strength becomes so strong that it is close to the plastic yield strength. However, the manifestation of plastic phenomena is likely to be limited to typical scales smaller than 10 nm.[53,54]

With these considerations we estimate the maximal rupture strength to be of the order $\sigma_R \approx 5$ GPa for our application due to the nanoscale of the pillar structures and the lack of protection from the atmosphere. For $H_0 = 1$ μm and 350 nm the critical horizontal shear stress is plotted versus the spacing in Fig. 9. The pillars withstand vertical stress better than shear. In the absence of any protection from the atmosphere, the long term shear resistance of the superamphiphobic layer is likely to be reduced by stress–corrosion phenomena.[55] Due to the cubic

(eqn (22)) or even R^4 (eqn (18)) dependence, increasing the particle size would drastically increase the mechanical stability.

We compare the critical horizontal stress to the horizontal capillary force acting at the rim of a drop. For a pillar to be stable the horizontal force given in eqn (10) needs to be lower than the value calculated by eqn (22):

$$F_h = 2\pi\gamma R\cos^2\frac{\Theta_r}{2}\cos\frac{\Theta_r^{app}}{2} < \frac{\pi\sigma_R R^3\sin^3\beta}{4H_0} \qquad (23)$$

An upper limit of the left hand side is $2\pi\gamma R$ leading to the stability criterion

$$\frac{\gamma}{\sigma_R} < \frac{R^2\sin^3\beta}{8H_0} \qquad (24)$$

The left hand side is of the order of $\gamma/\sigma_R \approx 10^{-11}$ m. With $H_0 = 1$ μm, $R = 50$ nm, and $\beta = 30°$ the right hand side is 4×10^{-11} m. The pillars should easily withstand the horizontal component of the surface tension.

Pillars at the rim of a drop are also subject to a vertical traction force, which is of the same order of magnitude as the horizontal component. Such force is thus comfortably smaller than the resistance of nanoscale silica pillars to uniaxial traction, which is comparable to the prediction of eqn (16) since $\sigma_R \approx 5$ GPa is close to $\sigma_y = 6.5$ GPa at the nanoscale.

Hydrodynamic drag

One potential application of superamphiphobic layers is in drag reduction. For superhydrophobic surfaces an effective slip has been calculated by partitioning the surface into regions of no-slip (solid–liquid interfaces) and no shear (the liquid–air interfaces).[56–60] In all cases the surfaces were assumed to be smooth and planar. For superamphiphobic layers we need to take hydrodynamic drag due to the overhanging topography into account.

As an example we consider the pressure-driven flow of a pure liquid in a cylindrical capillary of radius r_c and length Δx (Fig. 10). The capillary is coated at the inside with a super-amphiphobic layer. We assume that the radius of the capillary is large compared to all dimensions describing the super-amphiphobic layer ($a \ll r_c$, $H_0 \ll r_c$). Again we distinguish between the microscopic and macroscopic length scale. On the microscopic length scale the liquid in contact with the top of the pillar is assumed to follow the no-slip boundary condition. The velocity of the liquid parallel to the surface at zero distance is assumed to be zero. In between the pillars we assume that the liquid–vapor interface is not able to hold any shear (perfect slip). Macroscopically, that is on a length scale much larger than the pillar size and spacing, this leads to an effective slip length.

In the steady state the force caused by the applied pressure to the liquid in the capillary is $\pi r_c^2 \Delta P$. It is balanced by the hydrodynamic drag force $2\pi r_c \sigma_h \Delta x$. Equating both leads to

$$\sigma_h = \frac{r_c}{2}\frac{\Delta P}{\Delta x} \qquad (25)$$

here σ_h is the horizontal shear stress caused by the viscous drag of the liquid on the stationary topmost particles.
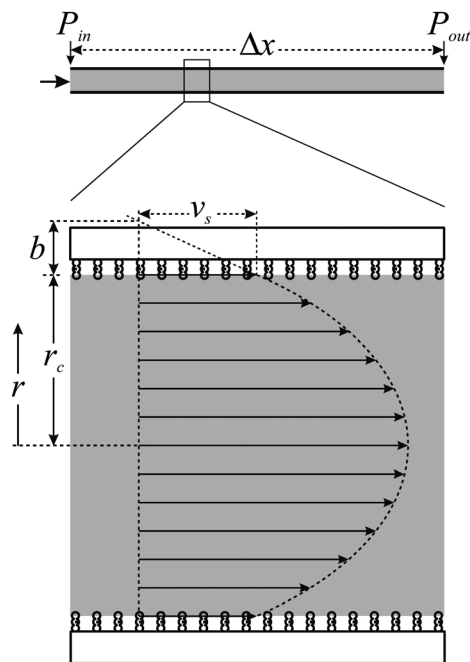
Fig. 10 Schematic of a capillary with liquid flowing from the left to the right (top). The pressure at the inlet, P_{in}, is higher than that at the outlet, P_{out}, with $\Delta P = P_{in} - P_{out}$. Bottom: cross-section along the capillary and the flow profile. Inside that capillary is coated with a superamphiphobic layer.

To relate the shear to microscopic parameters we assume that the drag force on the top sphere can be described by a modified Stokes friction:

$$F_d = 6\pi\eta R v_s f \tag{26}$$

here η is the viscosity of the liquid and v_s is the apparent, macroscopic slip velocity. The correction factor f is between 0.5 and 1.[61] For a half immersed sphere $f = 0.5$ (ref. 62), and for a fully immersed sphere $f = 1$. The transition between half and full immersed is not easy to describe and to our knowledge only numerical solutions have been reported.[63,64] That eqn (26) is a good approximation for the laminar flow of spheres attached to a fluid interface is supported by theory[62–65] and verified by drag and diffusion experiments on single macro-,[61,62,66] micro-[67,68] and nanospheres[69] at liquid–fluid interfaces.

From eqn (26) the shear stress is

$$\sigma_h = \frac{6\pi\eta R f}{A_0} v_s \tag{27}$$

Combining eqn (25) and (27) allows us to calculate the slip velocity as a function of the applied pressure gradient, sphere radius, and distance between pillars:

$$v_s = \frac{1}{12\pi\eta f} \frac{r_c A_0}{R} \frac{\Delta P}{\Delta x} \tag{28}$$

The flow profile for the pressure-driven flow is parabolic

$$v = v_s + \frac{(r_c^2 - r^2)}{4\eta} \frac{\Delta P}{\Delta x} \tag{29}$$

where r is the radial coordinate. The effective slip length b can be calculated by extrapolating the velocity gradient $|dv/dr|$ at $r \rightarrow r_c$:

$$b = \frac{v_s}{|dv/dr(r_c)|} = \frac{2\eta v_s}{r_c} \frac{1}{\Delta P/\Delta x} = \frac{1}{6\pi f} \frac{A_0}{R} \tag{30}$$

The slip length is defined as the distance beyond the solid–liquid interface at which the liquid velocity extrapolates to zero. To be precise, the solid–liquid interface in the Cassie state is just below the top sphere of the pillars. The effective slip length scales with a^2/R (Fig. 4C) since $A_0 \propto a^2$, which agrees with eqn (14) in ref. 70. It does not depend on the viscosity or the capillary radius.

The reduced drag at the wall of the capillary leads to an increased flow of[71]

$$\frac{dV}{dt} = \frac{\pi r_c^4}{8\eta} \frac{\Delta P}{\Delta x} + v_s \pi r_c^2 = \frac{\pi r_c^4}{8\eta} \frac{\Delta P}{\Delta x} \left(1 + \frac{4b}{r_c}\right) \tag{31}$$

The first term is the Hagen–Poiseuille flow, the second adds a plug flow with velocity v_s. The relative flow enhancement is proportional to the slip length divided by the radius of the capillary. In order to reduce drag a^2/R should be as large as possible.

The flow through a capillary is proportional to the applied pressure ΔP. If P_{in} exceeds the impalement pressure the liquid will invade the superamphiphobic layer. Once it locally passed from the Cassie to the Wenzel state, the transition will propagate through the whole capillary,[72] unless prevented by additional barriers. Therefore, impalement has to be prevented. Optimizing capillaries with respect to the pressure-driven flow is a compromise between increasing slip and allowing for a high impalement pressure. Increasing slip would demand a high value of a^2/R. Preventing impalement would require just the opposite. If we take into account the maximal applicable pressure as given by eqn (6) we get for the maximum flow before impalement:

$$\frac{dV}{dt} = \frac{\pi r_c^3}{8\eta} \frac{2\pi\gamma}{\Delta x} \sin^2 \frac{\Theta_a}{2} \left(\frac{r_c R}{a^2} + \frac{2}{3\pi f}\right) \tag{32}$$

The first term in brackets accounts for conventional Hagen–Poiseuille flow while the second is the enhancement due to slip. Slip only facilitates flow significantly if

$$\frac{r_c R}{A_0} < \frac{2}{3\pi f} \approx 0.4 \tag{33}$$

Thus for thin capillaries such as in microfluidic applications slip due to superamphiphobicity may become important. It is, however, unlikely that mass transport of liquids through thick pipes will be significantly affected.

To demonstrate this effect we calculated the pressure-driven flow through a capillary of 10 cm length which is coated at the inside with an array of pillars of spheres of $R = 0.5$ μm (Fig. 11). Two pillar spacings, a, were considered: 5 μm and 10 μm. With $a = 10$ μm the slip length is $b = 21$ μm and the impalement pressure is $P = 413$ Pa; $\gamma = 0.04$ N m^{-1}, $\Theta = 70°$ and $f = 0.5$ were chosen as typical parameters. For $a = 5$ μm the corresponding values are $b = 5.3$ μm and $P = 1650$ Pa. When applying a pressure to a microcapillary with a relatively small radius of $r_c =$
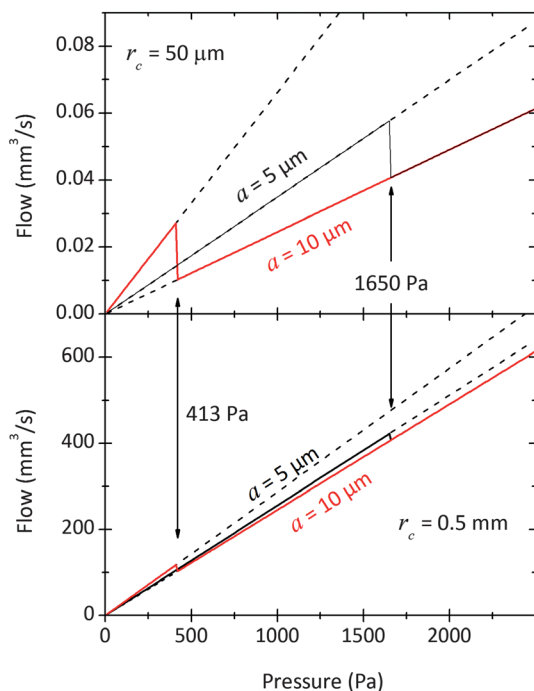
Fig. 11 Flow through a cylindrical capillary calculated with eqn (32) *versus* applied pressure for a radius $r_c = 50$ μm (top) and 0.5 mm (bottom). $\Delta x = 10$ cm, $R = 0.5$ μm, $a = 5$ (black) and 10 μm (red). Other parameters: $\gamma = 0.04$ N m^{-1}, $\Theta_a = 70°$, $\eta = 0.001$ Pa s, $f = 0.5$. Discontinuities mark the Cassie-to-Wenzel transition.

50 μm (Fig. 11, top), the flow increases linearly (eqn (31)). For the capillary with $a = 10$ μm the slope of this increase is higher because of the higher slip length. Once the impalement pressure of 413 Pa has been reached, the liquid passes the Cassie-to-Wenzel transition. The slip length is strongly reduced and practically goes to zero. Flow is described by the well-known law of Hagen–Poiseuille. For the narrower spacing ($a = 5$ μm) the Cassie-to-Wenzel transition is shifted to a higher impalement pressure. For a capillary of 0.5 mm radius (Fig. 11, bottom) qualitatively the same dependencies are obtained. Flow enhancement is, however, relatively low for both values of a.

The largest shear stress induced by hydrodynamic drag on the superamphiphobic layer in the considered examples is obtained for the larger capillary tube ($r_c = 0.05$ mm) and the smallest spacing a between pillars ($a = 5$ μm). Considering a pressure drop corresponding to the impalement pressure $P = 1650$ Pa over the tube length of 10 cm, the shear stress can be estimated to be 4 Pa from eqn (25). It is not a concern for the mechanical stability of the pillars.

In this context we would like to mention a related effect which reduces effective slip length. It is well established that surface active molecules adsorbed at the liquid–vapor interface change the full-slip to a no-slip boundary condition due to the Marangoni effect.[73–81] The surface active molecules can be deliberately added surfactants, but also contaminations. The flowing liquid creates concentration gradients in the adsorbed species. The resulting Marangoni effect counteracts the pressure driven flow. Marangoni effects[73] also delay the rise of bubbles in surfactant solutions,[74–77] stabilizes foam films[78–80] or

enhances repulsive hydrodynamic force between fluid interfaces.[82] They are active even at very low concentrations. In our case, the Marangoni effect would delay the flow of liquid between the pillars.

Conclusions

Arrays of vertical pillars of spheres, which are partially sintered together, can form apparent contact angles Θ^{app} above 150° even though the material's contact angle Θ is below 90°. Θ^{app} above 150° is obtained by pinning of the liquid surface at the underside of the top sphere resulting in a Cassie state. The impalement pressure determined by depinning is given by eqn (6) and increases with R/a^2.

By balancing forces at the rim of a drop, the material's contact angle could be related to the apparent contact angle. For a given material's contact angle the apparent receding contact angle is given by eqn (11) or (12). Θ_r^{app} increases with increasing a/R. The apparent contact angle depends on the direction of wetting or dewetting because for two-dimensional crystalline arrays the effective spacing between rows of pillars depends on the direction.

The superamphiphobic layers reduce drag and enhance the flow as long as the liquid remains in the Cassie state. To describe drag reduction we calculate the apparent slip length to be $\approx a^2/(3\pi R)$ (eqn (30)). Drag reduction is, however, only effective in microscopic channels.

For all applications where the use of superamphiphobic surfaces is limited to the Cassie state, silica glass pillars would be able to sustain the normal and shear stresses caused by capillary and drag forces. To increase the stability of superamphiphobic surfaces with respect to shear, R^3/a^2 should be as high as possible.

Acknowledgements

References

1 X. Yao, Y. L. Song and L. Jiang, *Adv. Mater.*, 2011, **23**, 719–734.
2 K. Watanabe and H. Udagawa, *AIChE J.*, 2001, **47**, 256–262.
3 S. Gogte, P. Vorobieff, R. Truesdell, A. Mammoli, F. van Swol, P. Shah and C. J. Brinker, *Phys. Fluids*, 2005, **17**, 051701.
4 J. Drappier, T. Divoux, Y. Amarouchene, F. Bertrand, S. Rodts, O. Cadot, J. Meunier and D. Bonn, *Europhys. Lett.*, 2006, **74**, 362–368.
5 C. Lee and C. J. Kim, *Langmuir*, 2009, **25**, 12812–12818.
6 B. Woolford, J. Prince, D. Maynes and B. W. Webb, *Phys. Fluids*, 2009, **21**, 085106.
7 G. McHale, M. I. Newton and N. J. Shirtcliffe, *Soft Matter*, 2010, **6**, 714–719.
8 J. P. Rothstein, *Annu. Rev. Fluid Mech.*, 2010, **42**, 89–109.
9 W. Barthlott and C. Neinhuis, *Planta*, 1997, **202**, 1–8.
10 A. B. D. Cassie and S. Baxter, *Nature*, 1945, **155**, 21–22.

11 C. Dorrer and J. Rühe, *Soft Matter*, 2009, **5**, 51–61.

12 R. N. Wenzel, *Ind. Eng. Chem.*, 1936, **28**, 988–994.

13 W. Chen, A. Y. Fadeev, M. C. Hsieh, D. Öner, J. Youngblood and T. J. McCarthy, *Langmuir*, 1999, **15**, 3395–3399.

14 A. Tuteja, W. Choi, M. L. Ma, J. M. Mabry, S. A. Mazzella, G. C. Rutledge, G. H. McKinley and R. E. Cohen, *Science*, 2007, **318**, 1618–1622.

15 S. Herminghaus, *Europhys. Lett.*, 2000, **52**, 165–170.

16 S. Shibuichi, T. Yamamoto, T. Onda and K. Tsujii, *J. Colloid Interface Sci.*, 1998, **208**, 287–294.

17 A. Steele, I. Bayer and E. Loth, *Nano Lett.*, 2009, **9**, 501–505.

18 D. Xiong, G. J. Liu, L. Z. Hong and E. J. S. Duncan, *Chem. Mater.*, 2011, **23**, 4357–4366.

19 X. Deng, L. Mammen, H.-J. Butt and D. Vollmer, *Science*, 2012, **335**, 67–70.

20 E. Yoshida, *Colloid Polym. Sci.*, 2012, **290**, 525–530.

21 R. Dufour, M. Harnois, V. Thomy, R. Boukherroub and V. Senez, *Soft Matter*, 2011, **7**, 9380–9387.

22 L. L. Cao, T. P. Price, M. Weiss and D. Gao, *Langmuir*, 2008, **24**, 1640–1643.

23 K. Ellinas, A. Tserepi and E. Gogolides, *Langmuir*, 2011, **27**, 3960–3969.

24 T. Darmanin, F. Guittard, S. Amigoni, E. T. de Givenchy, X. Noblin, R. Kofman and F. Celestini, *Soft Matter*, 2011, **7**, 1053–1057.

25 J. Bico, C. Marzolin and D. Quéré, *Europhys. Lett.*, 1999, **47**, 220–226.

26 D. Bartolo, F. Bouamrirene, E. Verneuil, A. Buguin, P. Silberzan and S. Moulinet, *Europhys. Lett.*, 2006, **74**, 299–305.

27 C. Priest, T. W. J. Albrecht, R. Sedev and J. Ralston, *Langmuir*, 2009, **25**, 5655–5660.

28 P. Papadopoulos, X. Deng, L. Mammen, D. M. Drotlef, G. Battagliarin, C. Li, K. Müllen, K. Landfester, A. del Campo, H.-J. Butt and D. Vollmer, *Langmuir*, 2012, **28**, 8392–8398.

29 M. R. Flynn and J. W. M. Bush, *J. Fluid Mech.*, 2008, **608**, 275–296.

30 M. L. Blow and J. M. Yeomans, *Langmuir*, 2010, **26**, 16071–16083.

31 Q. D. Xie, J. Xu, L. Feng, L. Jiang, W. H. Tang, X. D. Luo and C. C. Han, *Adv. Mater.*, 2004, **16**, 302–305.

32 C. W. Extrand, *Langmuir*, 2002, **18**, 7991–7999.

33 B. He, N. A. Patankar and J. Lee, *Langmuir*, 2003, **19**, 4999–5003.

34 C. W. Extrand, *Langmuir*, 2006, **22**, 1711–1714.

35 M. Nosonovsky, *Langmuir*, 2007, **23**, 3157–3161.

36 A. Tuteja, W. Choi, J. M. Mabry, G. H. McKinley and R. E. Cohen, *Proc. Natl. Acad. Sci. U. S. A.*, 2008, **105**, 18200–18205.

37 G. Whyman and E. Bormashenko, *Langmuir*, 2011, **27**, 8171–8176.

38 P. G. de Gennes, *Rev. Mod. Phys.*, 1985, **57**, 827–863.

39 M. Reyssat, J. M. Yeomans and D. Quéré, *Europhys. Lett.*, 2008, **81**, 26006.

40 N. A. Patankar, *Langmuir*, 2010, **26**, 8941–8945.

41 A. Scheludko, B. V. Toshev and D. T. Bojadjiev, *J. Chem. Soc., Faraday Trans. 1*, 1976, **72**, 2815–2828.

42 C. Huh and S. G. Mason, *Can. J. Chem.*, 1976, **54**, 969–978.

43 M. Preuss and H.-J. Butt, *J. Colloid Interface Sci.*, 1998, **208**, 468–477.

44 G. D. Yarnold, *Proc. Phys. Soc., London*, 1946, **58**, 120–125.

45 K. A. Brakke, *Philos. Trans. R. Soc., A*, 1996, **354**, 2143–2157.

46 J. L. Hilden and K. P. Trumble, *J. Colloid Interface Sci.*, 2003, **267**, 463–474.

47 L. A. Slobozhanin, J. I. D. Alexander, S. H. Collicott and S. R. Gonzalez, *Phys. Fluids*, 2006, **18**, 082104.

48 L. Gao and T. J. McCarthy, *Langmuir*, 2007, **23**, 3762–3765.

49 B. M. Mognetti and J. M. Yeomans, *Langmuir*, 2010, **26**, 18162–18168.

50 R. Lacroix, G. Kermouche, J. Teisseire and E. Barthel, *Acta Mater.*, 2012, **60**, 5555–5566.

51 A. A. Griffith, *Philos. Trans. R. Soc., A*, 1920, **221**, 163–198.

52 C. R. Kurkjian, P. K. Gupta, R. K. Brow and N. Lower, *J. Non-Cryst. Solids*, 2003, **316**, 114–124.

53 G. Brambilla and D. N. Payne, *Nano Lett.*, 2009, **9**, 831–835.

54 K. Han, M. Ciccotti and S. Roux, *EPL*, 2010, **89**, 66003.

55 M. Ciccotti, *J. Phys. D: Appl. Phys.*, 2009, **42**, 214006.

56 J. R. Philip, *J. Appl. Math. Phys.*, 1972, **23**, 960–968.

57 E. Lauga and H. A. Stone, *J. Fluid Mech.*, 2003, **489**, 55–77.

58 C. Ybert, C. Barentin, C. Cottin-Bizonne, P. Joseph and L. Bocquet, *Phys. Fluids*, 2007, **19**, 123601.

59 C. Lee, C. H. Choi and C. J. Kim, *Phys. Rev. Lett.*, 2008, **101**, 064501.

60 J. J. Zhou, A. V. Belyaev, F. Schmid and O. I. Vinogradova, *J. Chem. Phys.*, 2012, **136**, 194706.

61 J. T. Petkov, N. D. Denkov, K. D. Danov, O. D. Velev, R. Aust and F. Durst, *J. Colloid Interface Sci.*, 1995, **172**, 147–154.

62 B. Radoev, M. Nedjalkov and V. Djakovich, *Langmuir*, 1992, **8**, 2962–2965.

63 H. Brenner and L. G. Leal, *J. Colloid Interface Sci.*, 1978, **65**, 191–209.

64 T. M. Fischer, P. Dhar and P. Heinig, *J. Fluid Mech.*, 2006, **558**, 451–475.

65 K. D. Danov, R. Aust, F. Durst and U. Lange, *Chem. Eng. Sci.*, 1995, **50**, 263–277.

66 K. Zahn, J. M. Méndez-Alcaraz and G. Maret, *Phys. Rev. Lett.*, 1997, **79**, 175–178.

67 Z. P. Liang, X. D. Wang, D. J. Lee, X. F. Peng and A. Su, *J. Phys.: Condens. Matter*, 2009, **21**, 464117.

68 M. Sickert, F. Rondelez and H. A. Stone, *Europhys. Lett.*, 2007, **79**, 66005.

69 D. P. Wang, S. Yordanov, H. M. Paroor, A. Mukhopadhyay, C. Y. Li, H. J. Butt and K. Koynov, *Small*, 2011, **7**, 3502–3507.

70 L. Bocquet and J. L. Barrat, *Soft Matter*, 2007, **3**, 685–693.

71 E. W. Washburn, *Phys. Rev.*, 1921, **17**, 273–283.

72 C. Semprebon, S. Herminghaus and M. Brinkmann, *Soft Matter*, 2012, **8**, 6301–6309.

73 V. G. Levich and V. S. Krylov, *Annu. Rev. Fluid Mech.*, 1969, **1**, 293–316.

74 R. Clift, J. R. Grace and W. E. Weber, *Bubbles, Drops, and Particles*, Academic Press, New York, 1978.

75 Y. Pawar and K. J. Stebe, *Phys. Fluids*, 1996, **8**, 1738–1751.

76 B. Cuenot, J. Magnaudet and B. Spennato, *J. Fluid Mech.*, 1997, **339**, 25–53.

77 S. Takagi, T. Ogasawara and Y. Matsumoto, *Philos. Trans. R. Soc., A*, 2008, **366**, 2117–2129.

78 K. J. Mysels, K. Shinoda and S. Frankel, *Soap Films*, Pergamon Press, London, 1959.

79 T. T. Traykov and I. B. Ivanov, *Int. J. Multiphase Flow*, 1977, **3**, 471–483.

80 S. I. Karakashev and A. V. Nguyen, *Colloids Surf., A*, 2007, **293**, 229–240.

81 O. Manor, I. U. Vakarelski, X. S. Tang, S. J. O'Shea, G. W. Stevens, F. Grieser, R. R. Dagastine and D. Y. C. Chan, *Phys. Rev. Lett.*, 2008, **101**, 024501.

82 D. Y. C. Chan, O. Manor, J. N. Connor and R. G. Horn, *Soft Matter*, 2008, **4**, 471–474.